Comparing continuum and direct fiber models of soft tissues.
An ocular biomechanics example reveals that continuum models may artificially disrupt the strains at both the tissue and fiber levels

Xuehuan He[1], Mohammad R. Islam [1,3],
Fengting Ji[1,2], Bingrui Wang[1], Ian A. Sigal [1, 2] *

[1] Department of Ophthalmology, University of Pittsburgh, Pittsburgh, PA, USA
[2] Department of Bioengineering, University of Pittsburgh, Pittsburgh, PA, USA
[3] Department of Mechanical Engineering, University of Texas Rio Grande Valley, Edinburg TX, USA

Short Title: Comparing continuum and direct fiber models of the ONH.

* Correspondence: Ian A. Sigal, Ph.D.

Laboratory of Ocular Biomechanics

Department of Ophthalmology, University of Pittsburgh Medical Center, UPMC Mercy Pavilion,

1622 Locust Street, Rm 7.382, Pittsburgh, PA, USA. 15219.

Email: ian@OcularBiomechanics.com

www.OcularBiomechanics.org

Disclosures: X He: None; MR Islam: None; F Ji: None; B Wang: None; I.A. Sigal, None.

Keywords: Collagen, Fiber, Eye, Optic nerve head, Sclera, continuum mechanics, fiber mechanics, Biomechanics, finite element modeling

Abstract

Collagen fibers are the main load-bearing component of soft tissues but difficult to incorporate into models. Whilst simplified homogenization models suffice for some applications, a thorough mechanistic understanding requires accurate prediction of fiber behavior, including both detailed fiber-level strains and long-distance transmission. Our goal was to compare the performance of a continuum model of the optic nerve head (ONH) built using conventional techniques with a fiber model we recently introduced which explicitly incorporates the complex 3D organization and interaction of collagen fiber bundles [1]. To ensure a fair comparison, we constructed the continuum model with identical geometrical, structural, and boundary specifications as for the fiber model. We found that: 1) although both models accurately matched the intraocular pressure (IOP)-induced globally averaged displacement responses observed in experiments, they diverged significantly in their ability to replicate specific 3D tissue-level strain patterns. Notably, the fiber model faithfully replicated the experimentally observed depth-dependent variability of radial strain, the ring-like pattern of meridional strain, and the radial pattern of circumferential strain, whereas the continuum model failed to do so; 2) the continuum model disrupted the strain transmission along each fiber, a feature captured well by the fiber model.

These results demonstrate limitations of the conventional continuum models that rely on homogenization and affine deformation assumptions, which render them incapable of capturing some complex tissue-level and fiber-level deformations. Our results show that the strengths of explicit fiber modeling help capture intricate ONH biomechanics. They potentially also help modeling other fibrous tissues.

Statement of Significance

Understanding the mechanics of fibrous tissues is crucial for advancing knowledge of various diseases. This study uses the ONH as a test case to compare conventional continuum models with fiber models that explicitly account for the complex fiber structure. We found that the fiber model captured better the biomechanical behaviors at both the tissue level and the fiber level. The insights gained from this study demonstrate the significant potential of fiber models to advance our understanding of not only glaucoma pathophysiology but also other conditions involving fibrous soft tissues. This can contribute to the development of therapeutic strategies across a wide range of application

1.INTRODUCTION

Glaucoma, a leading cause of irreversible blindness worldwide [2, 3], is a progressive optic neuropathy characterized by optic disc excavation and the loss of retinal ganglion cell axons that transmit visual information from the eye to the brain [4, 5]. Clinical and experimental evidence indicates that the initial site of injury in glaucoma is the ONH, in the posterior pole [6]. Elevated IOP is one of the main risk factors for glaucomatous neural tissue damage, and every current treatment is based on lowering IOP. The mechanisms by which IOP translates into neural tissue damage remain unclear [7-9].

Understanding ONH sensitivity to IOP and thus individual susceptibility to glaucoma rests, in turn, in understanding how the tissues of the ONH region manage to bear biomechanical loads. Biomechanical support to the ONH region is provided by the collagenous connective tissues of the lamina cribrosa (LC) within the scleral canal, and the adjacent peripapillary sclera and the dura and pia maters [10]. The variability in individual susceptibility to IOP-related glaucomatous damage is thought to be due, at least in part, to differences in the mechanical behavior of the ONH tissues between individuals [11]. The desire to understand the sensitivity to IOP and susceptibility to glaucoma spurred the development of computational models that can capture the mechanical behavior of the tissues and the complex anatomy of the region. Early models simplified the tissues as linear, isotropic and homogeneous [12-17] or phenomenologically nonlinear [18]. Since collagen fibers are the primary load-bearing component of the ONH tissues, there has been great interest in developing computational models that can capture accurately the mechanical behavior of fibrous tissues. ONH models have thus advanced to incorporate inhomogeneous, anisotropic and nonlinear characteristics in some cases with fiber information derived from experiments [19-25].

Recent progress in imaging technology, specifically polarized light microscopy (PLM) [26-30] and its high speed variations [31, 32], have enabled much improved visualization of the three-dimensional (3D) organization of collagen fiber bundles in the ONH [27, 28, 33]. Utilizing this detailed information, our research group has developed a direct fiber modeling framework that accounts for the complex 3D organization and continuity of the collagen fiber bundles as well as the interactions between fiber bundles, first for a small region of the sclera [34] and later for a wide region of the posterior pole incorporating the ONH, as shown in Figure 1 [1].

31   The direct fiber modeling framework employed in this model can be seen as an alternative
32   to the conventional continuum approaches which employ constitutive models that homogenize the
33   fibers and assume affine kinematics between individual fibers and macroscopic tissue deformation
34   [35], without accounting for fiber-fiber interactions. Elsewhere we have shown that ignoring
35   interweaving and fiber-fiber interactions can introduce substantial errors when estimating sclera
36   fiber mechanical properties using inverse fitting [36]. Continuum homogenized models, and even
37   highly simplified phenomenological models have been proven sufficient to capture gross and
38   generic mechanical behavior of the eye. However, a thorough mechanistic understanding of the
39   ONH region requires accurate prediction of fiber behavior, including both detailed fiber-level
40   strains and its long-distance transmission. Our goal in this study was to compare the performance
41   of a continuum model of ONH built using conventional techniques with the fiber model which
42   explicitly incorporates the complex 3D organization and interaction of collagen fiber bundles [1].
43   To ensure a fair comparison, we constructed the continuum model with identical geometrical,
44   structural, and boundary specifications as for the fiber model.

45   Specifically, we considered the fiber structure-related parameters, such as fiber dispersion,
46   volume fraction, and orientation, as heterogeneous across the domain in the continuum model,
47   directly calculating them based on the fiber structure reconstructed in the fiber model. We
48   identified other material parameters following an inverse modeling approach to match the model
49   predictions with experimentally measured average displacements at 30mm Hg. The comparison
50   began with comparisons between the models' predictions and experimental measures in terms of
51   macro-level 3D tissue strain patterns and was followed by analyzing fiber-level long-distance
52   strain transmission; corresponding results will be presented and discussed.

2. METHODS

2.1 Continuum model geometry and boundary conditions.

We constructed a continuum model that aimed to mirror the fiber model introduced in [1] and shown in Figure 1, specifically in terms of geometries of the sclera, lamina cribrosa, neural tissue, pia mater and dura mater as well as the boundary conditions (Figure 2). The model was subjected to an elevated IOP of 30 mmHg. The same radial displacements (RD) used in the fiber model were applied to the continuum model's periphery to simulate the radial tension of the sclera due to IOP. Although our goal in this work focused on the mechanical behavior of the sclera, as it was in our previous papers [1, 34, 37], the continuum model incorporated a lamina cribrosa (LC) and retrolaminar neural tissues. These provide a robust set of boundary conditions.
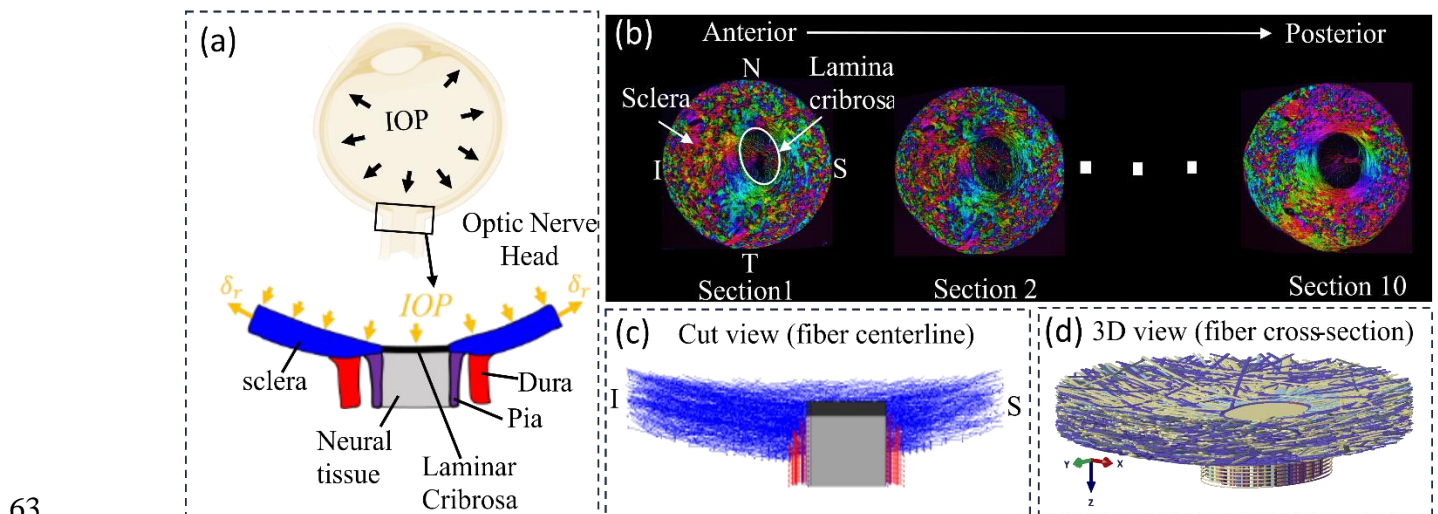
Figure 1. Schematic of an eye cross-section with an enlarged view of posterior sclera (blue), lamina cribrosa (black), retrolaminar neural tissue (grey), dura mater (red) and pia mater (purple) regions highlighted at the ONH. Boundary conditions included forces from IOP and displacements at the periphery. (b) Example images of serial coronal sections through the ONH of a pig eye from the anterior to posterior side. PLM was used to determine the collagen fiber orientation at each pixel [38]. Colors in the images indicate in-plane fiber orientation. Brightness indicates the strength of the signal. Low signal occurs when there is no birefringent material, no collagen, or the signal is blocked, for instance by pigment. The pig lamina cribrosa and scleral canal are elliptical with the major axis along the Nasal- Temporal (N-T) direction and the minor axis along the inferior-superior (I-S) direction. The Sections were stacked sequentially to construct a fiber

6

74   model for modelling the collagenous tissues in the ONH region [1]. (c) Longitudinal cut-model

75   view of the fiber model along the I-S direction with only bundle centerlines shown. (d) An

76   isometric view of the complete fiber model with full bundle width displayed.
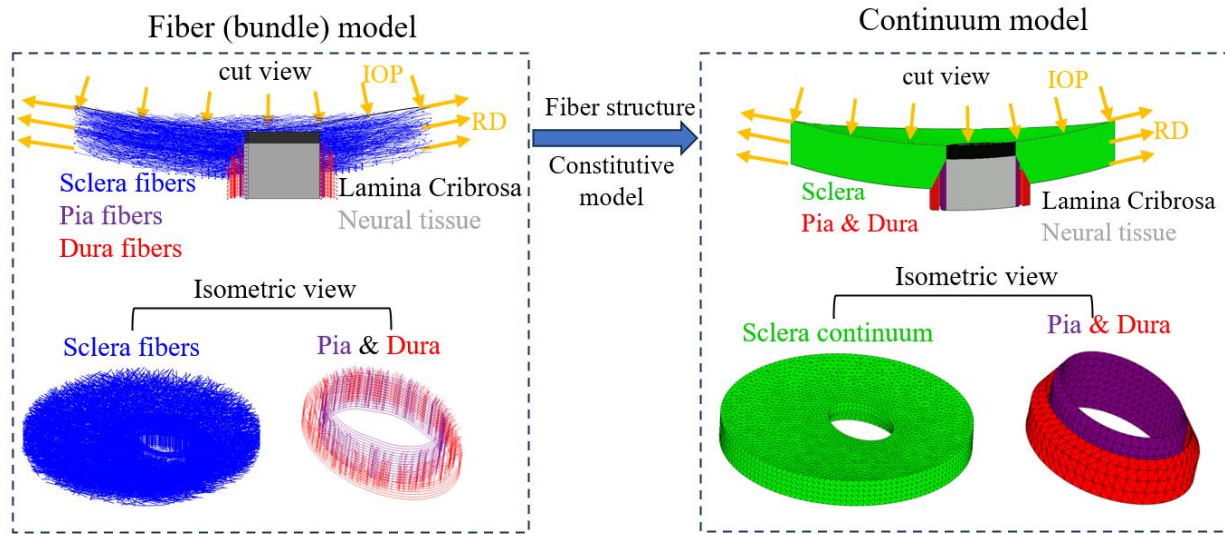
77

78   **Figure 2.** Schematic illustration of the geometry and boundary conditions of the fiber model and

79   the continuum models. The same boundary conditions were applied to both models to simulate an

80   inflation experiment. The continuum model was meshed using quadratic 10-nodded, tetrahedral

81   mixed-formulation elements (C3D10H in Abaqus). A coarser mesh was selected for the peripheral

82   sclera while a finer mesh was generated for the region where the peripapillary sclera, laminar

83   cribrosa, neural tissue, pia mater and dura mater are located. After a mesh refinement analysis, it

84   was decided that a mesh with ~78,000 elements and element size ranging from 0.1mm to 0.25mm

85   was used for the simulation.

86   **2.2 Continuum model material properties**

87   　　The sclera, pia mater and dura mater in the continuum model were assumed to be

88   incompressible, anisotropic, and heterogeneous. They were characterized using the Holzapfel-

89   Gasser-Ogden (HGO) strain energy function with one fiber family [39]. The form of strain energy

90   function, as implemented in ABAQUS, is given by:

91

92    $$W = W_{Ground} + W_{Fiber} \tag{1}$$

93   W is total strain energy density, W_{Fiber} is the strain energy density of the anisotropic

94   collagen fibers and W_{Ground} is the isotropic strain energy density of the non-collagenous ground

95   matrix.

96   The fiber strain energy density was modeled as:

97
$$W_{Fiber} = VF \frac{k_1}{2k_2} \sum_{\alpha=1}^{N} \{\exp[k_2 \langle E_\alpha \rangle^2] - 1\} \tag{2}$$

98   Where VF and k_1 represents the volume fraction and elastic modulus of collagen fibers.

99   k_2 is a material constant that governs how the stiffness of the fibers changes with the stretching of

100   the fiber.

101   The strain like quantity, E_α, is expressed as:

102
$$E_\alpha = \kappa(\overline{I_1} - 3) + (1 - 3\kappa)(\overline{I_4} - 1); \ \overline{I_4} = \boldsymbol{M_\alpha} \cdot \overline{\boldsymbol{C}} \boldsymbol{M_\alpha} \tag{3}$$

103   It represents the deformation of the fiber family with the mean direction, $\boldsymbol{M_\alpha}$, denoting as

104   a 3D unit vector and the fiber angular dispersion, κ. Here, $\overline{\boldsymbol{C}} = J^{-\frac{2}{3}}\boldsymbol{C}$ is the modified right Cauchy-

105   Green deformation tensor; and J is the determinant of the deformation gradient $\boldsymbol{F}$. $\overline{I_1}$ is the first

106   invariant of $\overline{\boldsymbol{C}}$; and $\overline{I_4}$ is the squared stretches in the mean fiber direction, $\boldsymbol{M_\alpha}$. This model

107   presumes that the orientation of the collagen fibers in each family is distributed rotationally

108   symmetrically with respect to the mean preferred orientation $\boldsymbol{M}(\theta, \phi)$. This rotational symmetry

109   implies that the fiber orientation distribution is independent of the elevation angle ϕ, i.e.,

110   $\rho(\boldsymbol{M}(\theta, \phi)) \to \rho(\theta)$. The parameter, κ, is then defined as follows:

111
$$k = \frac{1}{4} \int_0^\pi \rho(\theta) \sin^3(\theta) \, d\theta \tag{4}$$

112   The parameter κ takes values within the range [0, 1/3]. When $\kappa = 0$, fibers are completely

113   aligned in the mean fiber direction (no dispersion). When $\kappa = 1/3$, the fibers are randomly

114   distributed, and the material becomes isotropic.

115   The strain energy density equation for the ground material was modeled as a neo-Hookean

116   solid which has the form:

117
$$W_{Ground} = (1 - VF)C_{10}(\overline{I_1} - 3) + \frac{1}{D}\left(\frac{(J^{el})^2 - 1}{2} - lnJ^{el}\right) \tag{5}$$

8

118   C_{10} is a material constant defining the stiffness of the ground substance. D is the bulk
119   modulus which defines the compressibility of the material. J^{el} is the elastic volume ratio. The
120   incompressibility of collagenous tissue was accounted for by setting D as 0 and the utilize of
121   mixed-formulation element type C3D10H in Abaqus.
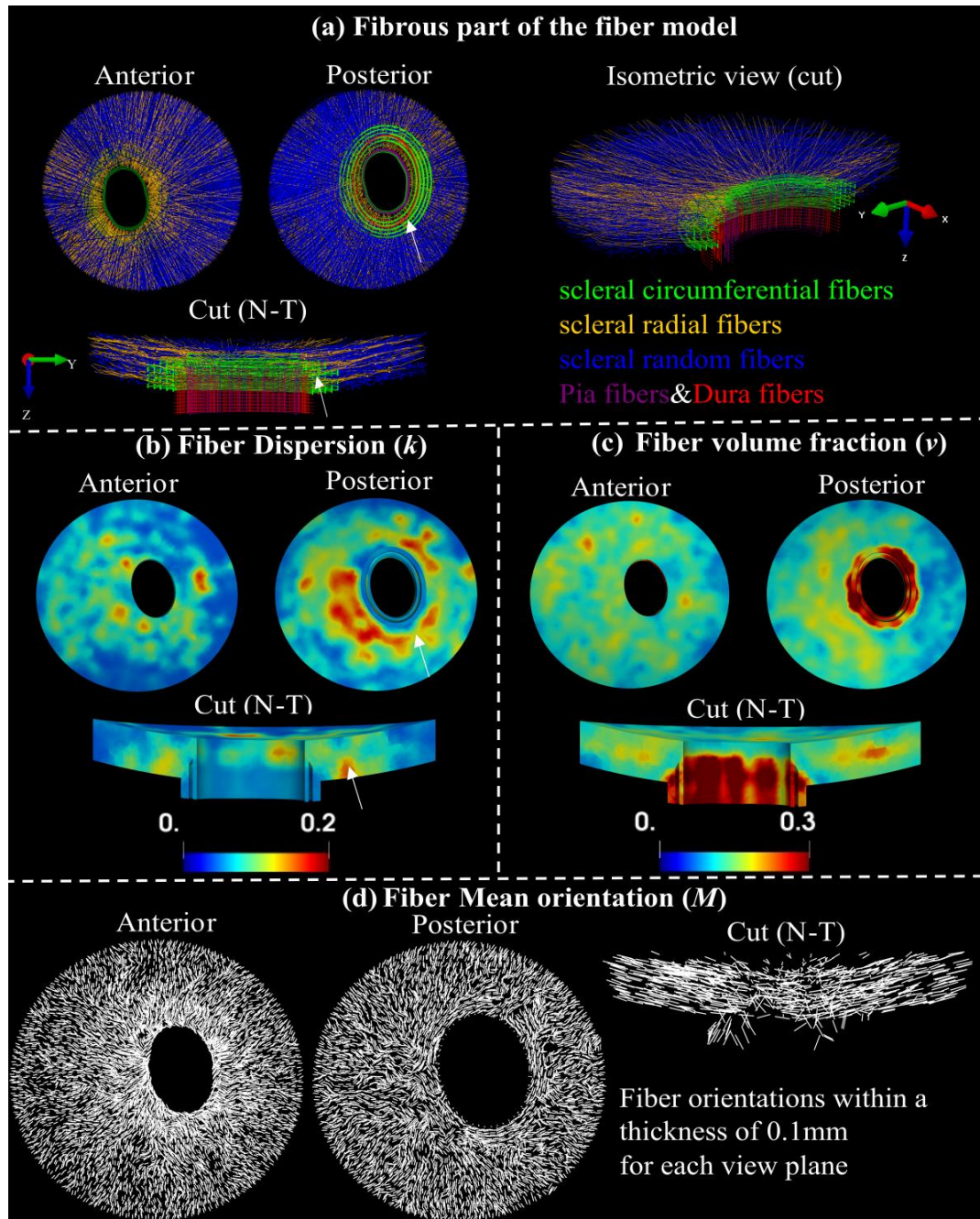
122   The lamina cribrosa (LC) and neural tissue (NT) regions were modeled as linear elastic
123   material (ELC = 0.1 MPa, ENT = 0.01 MPa), same as the fiber model.

2.2.1 Identification of heterogeneous fiber dispersion, volume fraction and mean orientation.

125   The fiber structure-related parameters of the HGO model, including fiber dispersion κ,
126   fiber volume fraction v, and mean fiber direction $\boldsymbol{M}$, were determined on an element-by-element
127   basis based on the fiber structure of the fiber model reconstructed from 10 PLM images of porcine
128   ONH coronal sections as shown in Figure 1. To faithfully represent the heterogeneous fiber
129   structural properties while maintaining the smoothness of material parameters in the tissue, in-
130   house code was developed to calculate element-wise values of these three parameters. Briefly, for
131   each element of the meshed sclera, pia and dura mater, neighboring elements whose center points
132   are within 0.4mm—twice the average element size—were selected along with this element as the
133   region of interest (ROI). Fiber segments within the ROI were then extracted. The fiber volume
134   fraction v was calculated as the ratio of the total fiber segments volume, considering the fiber
135   bundle cross-section, to the total volume of the ROI. The directions of these fiber segments were
136   fitted to a 3D π-periodic von Mises distribution to get the mean fiber direction vector $\boldsymbol{M}$ and the
137   concentration parameter b. The fiber dispersion κ was then related to b as:

$$k = \frac{1}{4} \int_0^\pi \rho(\theta, b) \sin^3(\theta)\, d\theta \qquad (6)$$

139   Here, $\rho(\theta, b)$ is the 2D π-periodic von Mises distribution. The derived distributions of
140   calculated fiber dispersion κ, fiber volume fraction v and mean fiber orientation $\boldsymbol{M}$ are shown in
141   Figure 3.

Figure 3. Fiber structure and contours of structure parameters. Visualization of entire fibrous regions of the fiber model with scleral random (blue), scleral radial (orange), and scleral circumferential (green), pia (purple) and dura (red) fibers in anterior view, posterior view, a sectional and an isometric cut view along the nasal-temporal (N-T) direction (a). Maps of fiber dispersion (b), fiber volume fraction (c), and mean fiber orientation (c) for these fibrous regions in anterior, posterior, and the sectional cut views. Note that the fiber dispersion here is inversely

10

149   related to its degree of anisotropy. The peripapillary scleral region (indicated by the white arrows)

150   consists of green circumferential fibers and other types of fibers (a), indicating a highly dispersed

151   or isotropic distribution of fibers in these regions, which is associated with higher fiber dispersion

152   (b).

2.2.2 Identification of optimized matrix modulus, fiber modulus and exponential parameter

153

154   The other three HGO constitutive parameters, including the modulus of matrix C_{10},

155   modulus of fibers u, and the exponential parameter k_2 for fibers, were regarded as homogeneous

156   across the tissue. These parameters were identified by inversely matching the IOP-induced

157   posterior average displacement of the nerve region and peripapillary sclera (PPS), as well as

158   average scleral canal expansion, with those derived from ex-vivo inflation experiments

159   documented in the literature [40]. To determine optimized parameter values, a grid table formed

160   by $C_{10} = [0.001 : 0.002 : 0.2]$, $u = [20 : 10 : 200]$, $k_2 = [50 : 50 : 1000]$ was tested. The group of

161   values that yielded the best match of simulated responses with the experimental data were regarded

162   as the optimized parameter values. The finite element simulation was performed using the FE

163   solver Abaqus/Standard. Customized code and the GIBBON toolbox [41] for MATLAB v2023

164   [42] were used for model pre/post-processing and inverse identification of optimized parameters.

165   The simulation results of the continuum model with $C_{10} = 0.013$, $u = 120$ and $k_2 = 500$

166   produced the best match with the experimental data in terms of posterior displacements of the

167   nerve region and PPS as well as horizontal sclera expansion. Figure 4 shows the predicted average

168   displacements (dashed lines) with identified optimized material parameters of a porcine ONH from

169   the fiber model (blue) and the continuum model (green) compared to the experimental

170   measurements of different porcine eyes (circle symbols) obtained from ref. [40]. Note that the

171   experimental displacements were measured over the ONH regions in the cross-section along the

172   nasal-temporal (N-T) meridian direction. The same regions of the models were utilized to measure

173   average model displacement. The shaded regions represent the standard deviation of experimental

174   measurements from multiple eyes (n = 12). Albeit there is a slight difference of the response curves,

175   the adjusted model predictions (solid lines) show excellent agreement with the experimental

176   responses for all measurements. As expected, the actual model, without adjustment (dashed grey

177   lines), does not match the experiments as well because of the difference in reference state. Please

178   see the study introducing the fiber model for more on this topic [1].
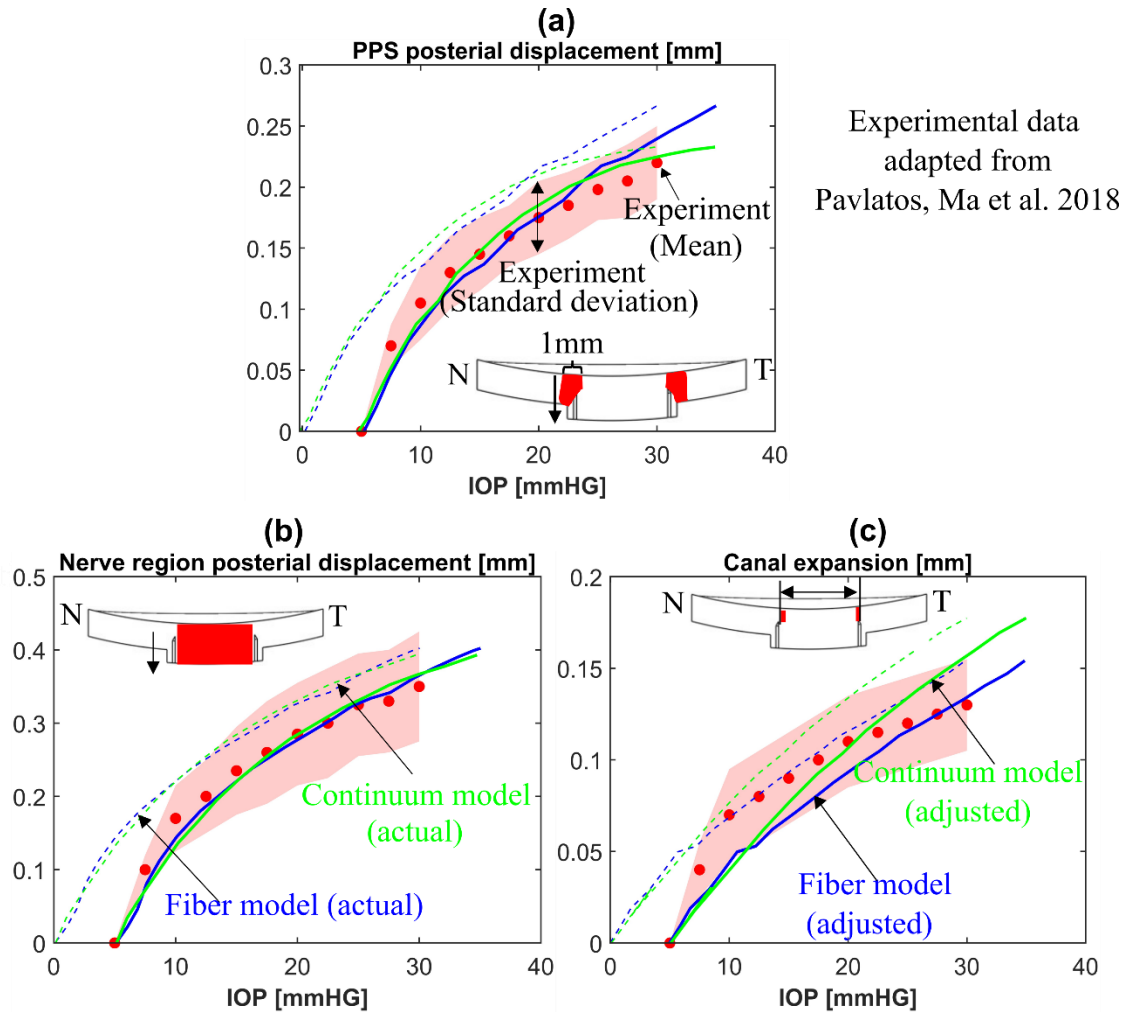
Figure 4. Mechanical validation of the fiber (blue lines) and continuum(green lines) models. The comparisons of (a) the mean posterior displacement of the porcine peripapillary sclera (PPS), (b) the mean posterior displacement of the optic nerve region (lamina cribrosa and neural tissue parts), and (c) the mean scleral canal expansion between the inflation experiments (circle symbols) from ref. [40] and the models (lines). Note that the specimen configurations at 5 mmHg were employed as the undeformed configuration for measuring ONH deformations in the experiments while the configuration at 0 mmHg was used as the undeformed configuration in the model. Therefore, the model responses are adjusted by 5 mm Hg in the IOP axis to account for differences in reference configurations. The shaded regions in (a)-(c) represent the standard deviation of experimental measurements for multiple porcine eyes (n = 12). The dashed and solid lines in (a)-(c) represent the actual and adjusted responses of the models, respectively. The insets in (a)-(c) indicate the regions used for calculating the mean posterior displacements and the canal expansion.

12

2.3 Comparison of strains between the continuum and the fiber models

As illustrated in Figure 5, we calculated and then compared both models in terms of the three-dimensional tissue-level strain patterns and fiber strains.
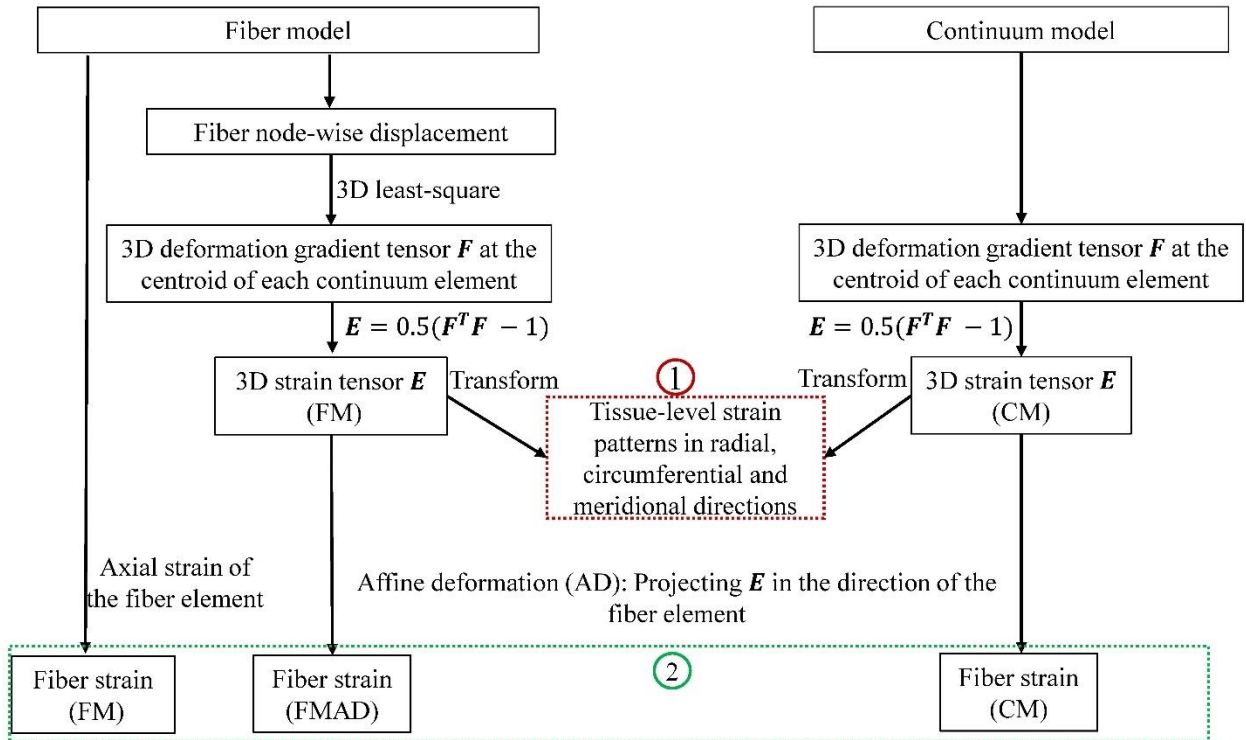
Figure 5. A flowchart showing the procedures in deriving 3D tissue-level strains (1) and fiber strains (2) for the fiber (FM) and continuum (CM) models. The deformation gradient tensor F in the CM was acquired directly from the simulation. For the FM, F was also calculated at the centroids of continuum elements to ensure consistent comparisons. The details of this calculation can be found in section 2.3.1. Tissue-level strains in radial, circumferential and meridional directions were computed by transforming the strain tensor EE from Cartesian coordinates to spherical coordinates, with further details on this transformation and direction conventions available in Section 2.3.1. In the FM, fiber strain refers to the axial strain of the fiber element, derived directly from simulation results. For the CM, fiber strain was determined by projecting the 3D strain tensor E along the fiber element direction, following the affine deformation (AD) assumption commonly used in continuum kinematics [35]. This approach relies on the affine deformation (AD) assumption in the continuum kinematics. Employing the same AD assumption,

13

208 fiber strain was also calculated based on the strain tensor derived from FM, and we refer this as

209 the fiber strain for the fiber model with affine deformation (FMAD).

2.3.1 Comparisons of three-dimensional tissue strain patterns in sclera

211 Several studies have reported the tissue-level 3D strain patterns of the ONH (lamina

212 cribrosa and neural tissue parts), and peripapillary sclera (PPS) derived from experimental inflation

213 tests [40, 43-46]. We calculated the 3D tissue strains in the radial, circumferential, and meridional

214 directions from the continuum and fiber models at 30 mm Hg, following the procedures illustrated

215 in Figure 5, and then compared their patterns with those reported in experimental studies.

216 For both models, the green strain tensor E at the centroid of each continuum element was

217 calculated as $E = 0.5(F^T F - 1)$ where F is the deformation gradient tensor. For the continuum

218 model, F was acquired directly from the simulation. For the fiber model, it was postprocessed

219 based on the displacements of fiber nodes derived from the simulation. For each element's centroid

220 in the continuum model, neighboring fiber nodes within 400um were selected and corresponding

221 displacements vectors in the Cartesian coordinate were denoted as U_i $(i = x, y, z)$. The

222 deformation gradient tensor F in the Cartesian coordinate was calculated as follows:

$$F = \begin{bmatrix} \dfrac{\partial U_x}{\partial x} + 1 & \dfrac{\partial U_x}{\partial y} & \dfrac{\partial U_x}{\partial z} \\ \dfrac{\partial U_y}{\partial x} & \dfrac{\partial U_y}{\partial y} + 1 & \dfrac{\partial U_y}{\partial z} \\ \dfrac{\partial U_z}{\partial x} & \dfrac{\partial U_z}{\partial y} & \dfrac{\partial U_z}{\partial z} + 1 \end{bmatrix} \qquad (7)$$

224 where the displacement gradients $\partial U_i / \partial U_j$ were obtained by a 3D least-squares method

225 [47, 48].

226 The derived Cartesian strain tensor E was transformed into spherical strain tensor E_{sph} in

227 the spherical coordinate via a transformation matrix T as $E_{sph} = TET^T$ [45, 49]. The T is given

228 by:

$$T = \begin{bmatrix} sin\theta cos\varphi & sin\theta sin\varphi & cos\theta \\ cos\theta cos\varphi & cos\theta cos\varphi & -sin\theta \\ -sin\varphi & cos\varphi & 0 \end{bmatrix} \qquad (8)$$

230   Where θ is the azimuth angle and φ is the elevational angle as shown in Figure 6. The

231   diagonal components of derived spherical strain tensor $\mathbf{E_{sph}}$ represent the normal strain in radial

232   E_r, meridional E_φ and circumferential E_θ direction as denoted in Figure 6, respectively.
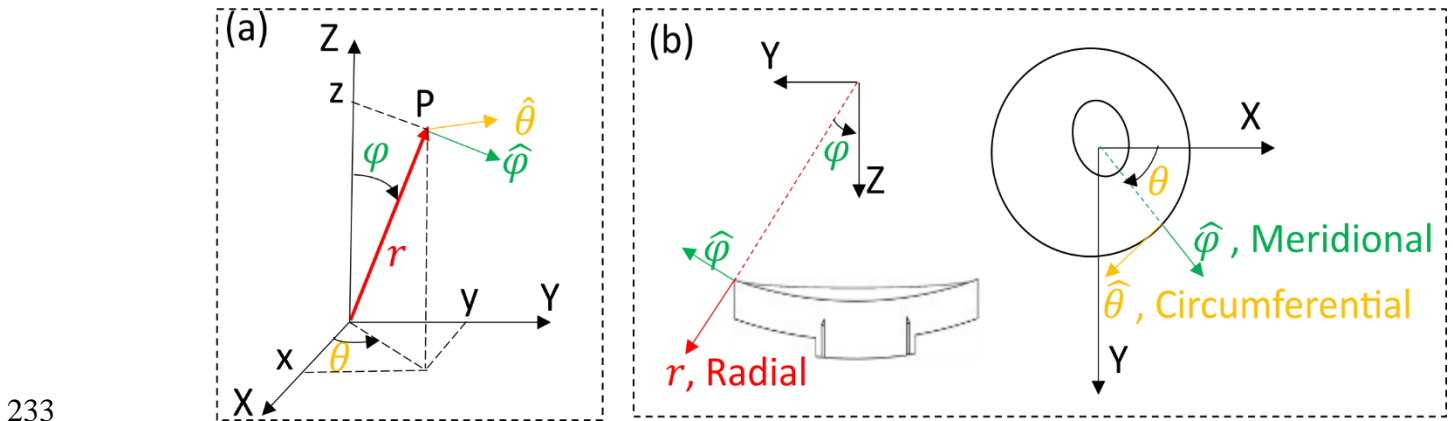
234   **Figure 6.**   (a): Schematic of the 3D cartesian coordinate (X, Y, Z) and spherical coordinate

235    $(\mathbf{r, \theta, \varphi})$ systems. (b): Illustration of the radial, meridional and circumferential directions for the

236   ONH model in cut view (N-T direction) and anterior view. The radial direction was defined to be

237   aligned with the through-thickness direction of the ONH, which agrees with the experimental data

238   **2.4 Comparison of fiber strains between the continuum and fiber models.**

239   We followed the procedures depicted in Figure 5 to calculate and compare fiber strains

240   between the CM, FM, and FMAD at 30 mm Hg. This comparison focused on the distribution of

241   fiber strains for fiber elements along each entire fiber in scleral fiber bundles. To quantify the

242   degree of variation in fiber strains, we calculated the standard deviations of fiber strains along each

243   entire fiber derived from the three models for all fibers.

15

244 **3. RESULTS**

245 **3.1 Comparison of three-dimensional tissue strains between the continuum and fiber models**

246   Predicted tissue-level radial strain patterns from the FM and CM were compared to

247 experimentally measured patterns from a human eye [46] (Figure 5). The experimentally measured

248 radial strains exhibited depth-dependent variability from the anterior to the posterior side, with

249 significant compression in the anterior, whereas the posterior side of the LC, NT and PPS were

250 less compressed or even stretched. In addition to the study shown in Figure 5. a, this pattern has

251 also been reported in another study for human sclera tissue [45]. The FM accurately replicated the

252 depth-dependent variation of the radial strain for the PPS, whereas the CM did not. It is important

253 to acknowledge that the LC and NT part, modeled as a continuum in both models, did not

254 reproduce the experimental radial strain patterns.

255   The FM also replicated some interesting features of circumferential and meridional strain

256 patterns observed experimentally from the posterior side of a human sclera [44], whereases the

257 CM failed to (Figure 8). Here, the circumferential strain seems to display a radial pattern, with

258 bands emanating from the scleral canal and extending outward in all directions. In contrast, the

259 meridional strain tends to follow a ring-like pattern, with large strains surrounding the scleral canal.

260 The FM effectively captured these contrasting patterns and the pronounced near-canal meridional

261 strains.
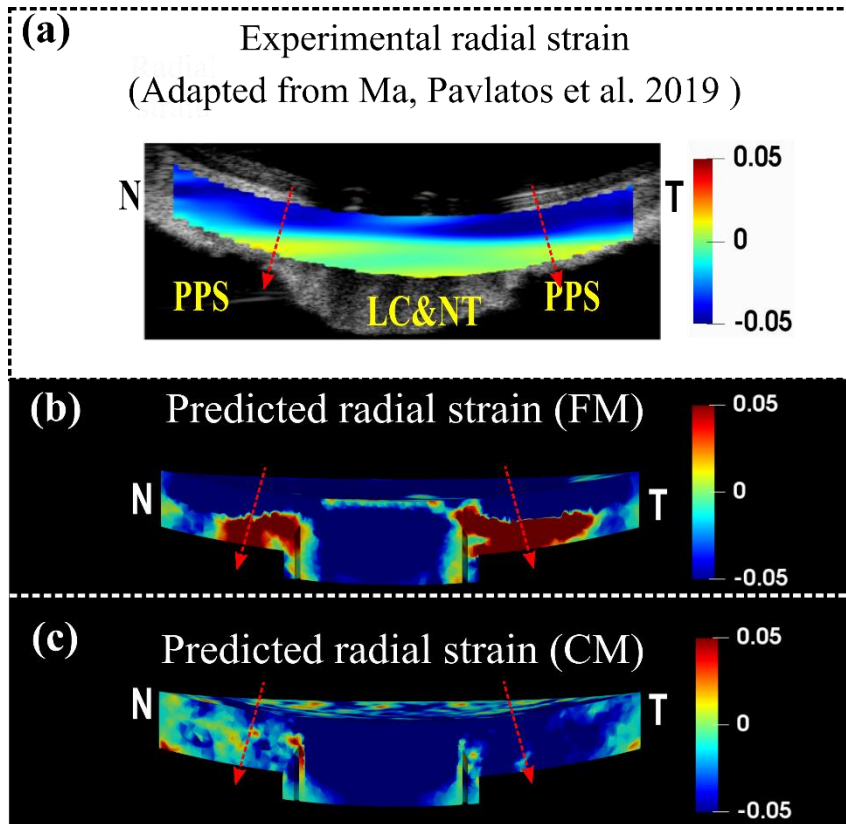
Figure 7. A comparison of the experimental (a) [46], the FM predicted (b) and the CM predicted (c) radial strains for the sagittal section of the optic nerve head along the Nasal-Temporal (NT) direction at 30 mm Hg. The red arrows indicate the direction of radial strain at through-thickness points, represented by corresponding dashed lines, which are oriented from anterior to posterior. The detailed direction convention can also be found in Figure 6. The experimental radial strain derived from a human eye exhibits depth-dependent variation, compressing more at the anterior and less, or stretching, at the posterior (a). Note that the fiber model faithfully replicated this pattern, but the continuum model failed to reflect it.

3.2 Comparison of fiber strains between the continuum and fiber models.

The fiber strains derived from the FM, CM and FMAD for fiber elements along each entire fiber are shown in Figure 9. Visually, the fiber strains in the FM appear quite smooth along each fiber but vary significantly in the CM and FMAD. This observation is further supported by the results of the standard deviations of fiber element strains along each fiber for all fibers, as shown in Figure 10. Overall, the fiber strains exhibit a much lower degree of variation in the FM than in the CM and FMAD along each fiber.

17
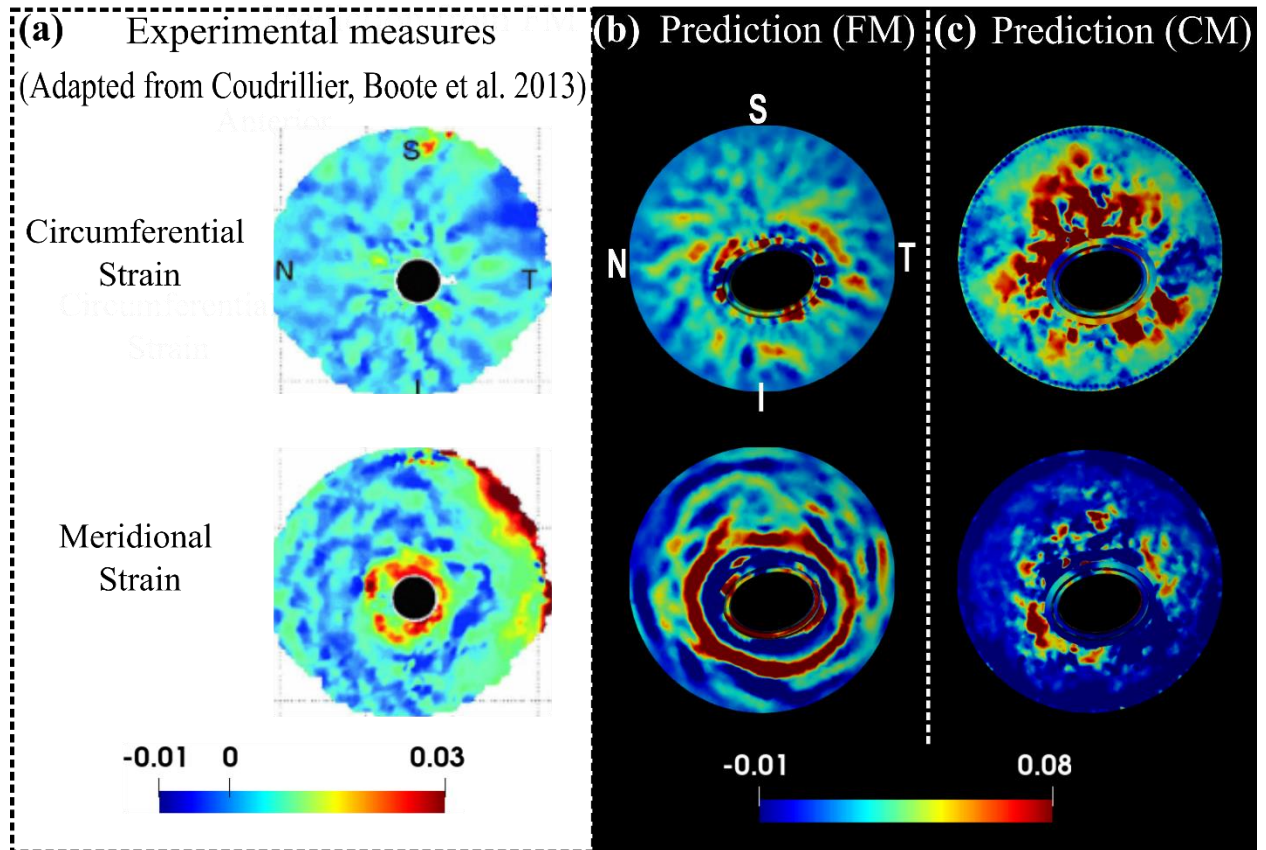
Figure 8. A comparison of the experimental (a) [44], the FM predicted (b) and the CM predicted (c) circumferential and meridional strain patterns from the posterior view of the ONH at 30 mm Hg. Detailed direction conventions for the circumferential and meridional strains are described in Figure 6. The plots of model predictions (b and c) were adjusted to align with the experimental plots in terms of the positions of the four quadrants: nasal (N), temporal (T), superior (S), and inferior (I). The experimental patterns, derived from a human sclera specimen [44], interestingly show contrasting behaviors: the circumferential strain radiates from the sclera canal, forming a pattern with outward-extending bands, whereas the meridional strain appears as a series of open, ring-shaped bands with high values concentrated near the canal. These contrasting patterns and pronounced near-canal meridional strains were accurately captured by the fiber model but not by the continuum model.
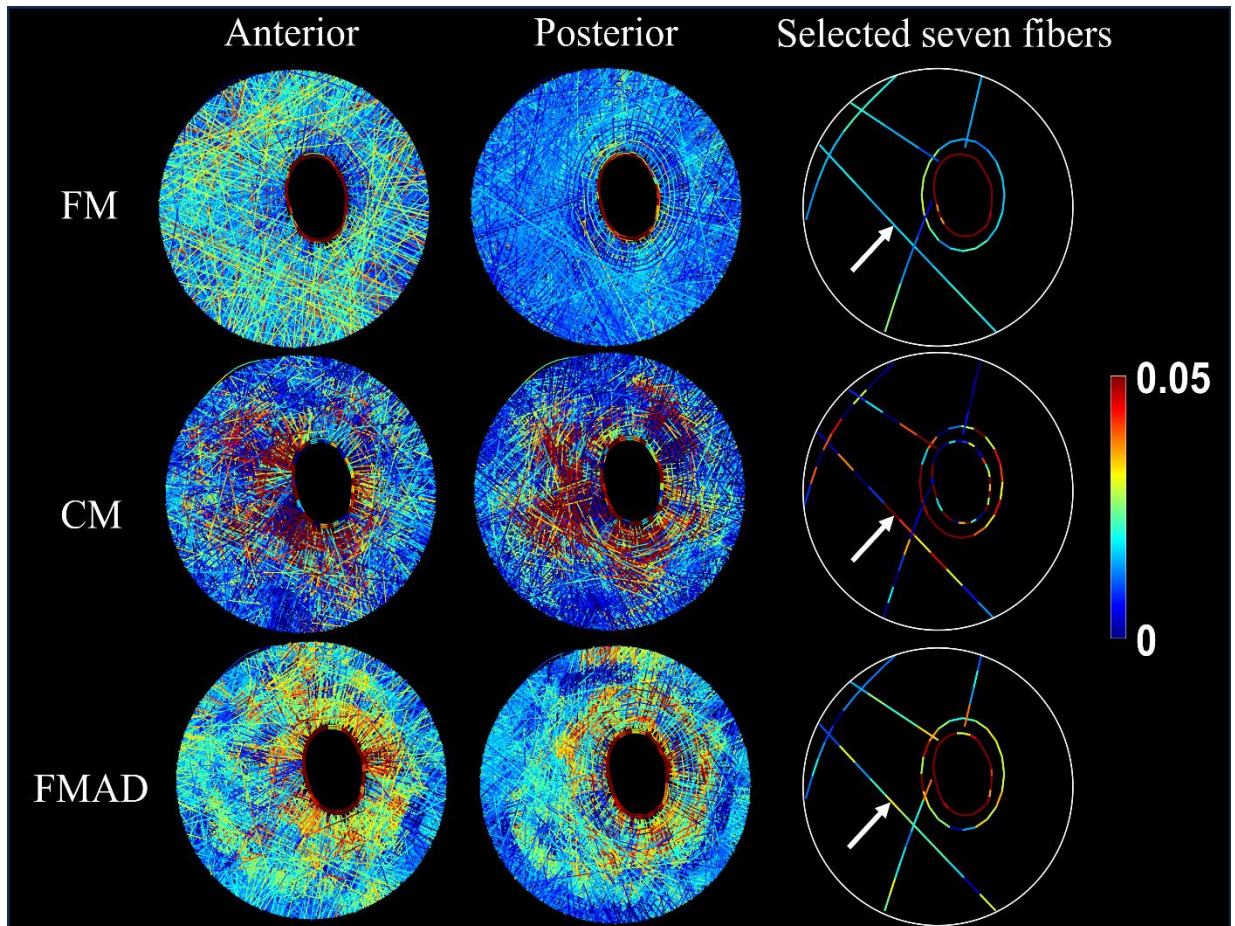
Figure 9. Visualization of fiber strains for all sclera fibers (anterior view in the first column and posterior view in the second column) and seven selected whole fibers (third columns) in FM, CM, and FMAD. The selection of seven fibers allows for a clearer investigation of the fiber strain changes along each fiber. Further information on the fiber strain calculation methodologies for each model can be found in Figure 5 and Section 2.3.1. Take the fiber indicated by the arrows as an example. Note how the smooth strains along the fiber in the FM were disrupted in the CM and FMAD due to the enforcement of affine deformation in calculating the fiber strains. Interestingly, the fiber strains within the FM exhibit depth-dependent variation, with larger strains evident in the anterior view and smaller strains in the posterior view. This variation appears to be less pronounced or absent in the CM and FMAD models.

19
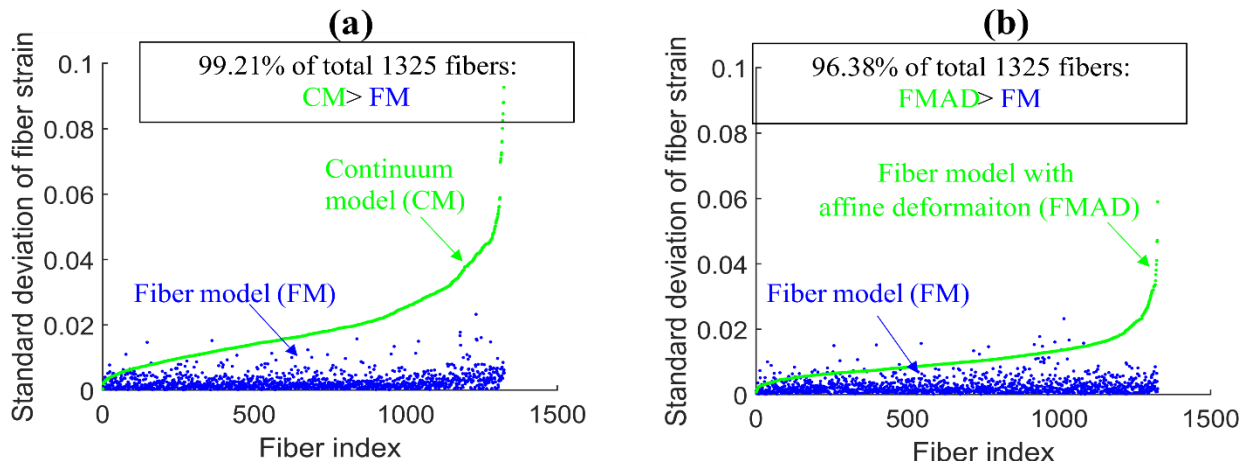
Figure 10. Scatterplots of the standard deviations of fiber element strains along each of the 1325 fibers derived from CM and FM in (a) and from FMAD and FM in (b). Fibers are indexed according to the standard deviation of fiber strains from the CM in (a) and FMAD in (b). The plots highlight that fiber strains from FM are notably consistent along each fiber (low standard deviations), with 97% of fibers from FM exhibiting standard deviations below 0.01.whereas those calculated enforcing affine deformation in continuum kinematics (CM and FMAD) show significantly more variability.

4. DISCUSSION

In this study, we employed the ONH as a test case to assess the biomechanical performance of our FM compared to a conventional CM developed using standard techniques. Our findings reveal that, while both models adequately matched the globally averaged displacement responses induced by IOP observed in experiments, they diverged dramatically in their ability to replicate specific 3D tissue-level strain patterns. Notably, the FM excelled in capturing the depth-dependent variability of radial strain, the ring-like pattern of meridional strain, and the radial pattern of circumferential strain —patterns which the CM failed to reproduce. Moreover, the FM preserved the smooth strain transmission along each fiber, in contrast to the conventional CM, which disrupted this transmission. Below, we discuss the motivation and rationale for the study as well as the significance of each finding.

Collagen fibers are the main load-bearing component of soft tissues but difficult to incorporate into models. Conventional CMs represent the collagenous fibers in soft tissues as homogenized continuum structures, which are effective for predicting macro-scale responses but lack the capacity to provide detailed fiber-level behaviors necessary to fully comprehend fibrous tissue biomechanics [22, 24, 44, 50]. To overcome these shortcomings, we have developed a FM that explicitly incorporates the complex 3D organization and interactions of collagen fiber bundles within the ONH. The motivation for this research is to highlight the significant advantages of our fiber model over conventional continuum models. By using the ONH as a test case, we aim to demonstrate that our model can more accurately predict both the intricate tissue-level strain patterns and the long-distance strain transmission along the fibers, which are crucial for advancing our understanding of fibrous tissue biomechanics and linking tissue biomechanics with cellular mechanobiology [51].

We acknowledge that the models we compare are distinct, by nature, and therefore that there will always be differences between them. Nevertheless, we contend that the comparison between them is fair, for the following reasons: Both models were developed with identical geometric and boundary specifications, ensuring a level basis for comparison When it comes to material properties, the two models account for the properties of the same fiber structure but intrinsically diverge in their approaches to representing it. The FM accurately reconstructed the fiber structure, assigning a linear stiffness to each fiber bundle. In contrast, the CM simplifies the

21

339   fiber structure into a homogenized continuum and employs an anisotropic, structurally motivated

340   constitutive model to account for the material properties. In this constitutive model, fiber structure-

341   related parameters—such as volume fraction, dispersion, and mean orientation were directly

342   calculated and assigned to each mesh element based on the detailed fiber structure used in the fiber

343   model. For each element, the region of interest (ROI) is defined as twice the average element size

344   to ensure inclusion of surrounding elements. This approach guarantees the smoothness of the

345   material domain and replicates the local structural properties as accurately as possible. Other

346   material parameters, including the modulus of the matrix and fibers, and the exponential parameter,

347   were assumed to be homogeneous across the domain. These parameters were inversely identified

348   by matching the model predictions with experimentally measured responses. It is important to note

349   that the assumption of homogeneity for these parameters is not arbitrary but follows standard

350   practice in these types of studies [19, 21, 23]. Furthermore, unlike previous studies that typically

351   rely on estimated parameter values from prior research, our study enhances the accuracy and

352   relevance of our models by employing an optimization process through inverse modeling, aligning

353   with the method used in determining fiber stiffness for the FM [1]. However, it is crucial to

354   recognize that despite our efforts to align the models as closely as possible, the two approaches

355   remain inherently distinct. No modeling approach can perfectly replicate another due to

356   fundamental differences. Thus, while our efforts ensure a fair comparison, they also highlight the

357   unique contributions and limitations inherent in each modeling approach.

358   Our results demonstrated that both models performed equally well in replicating the

359   experimentally measured nonlinear IOP-induced average displacement responses of the ONH

360   through an inverse modeling approach, with one parameter optimized for the FM and three for the

361   CM (Figure 4). However, significant differences emerged when it came to capturing 3D tissue-

362   level strain patterns. The FM, despite using only one parameter to represent the linear, isotropic

363   fiber bundles modeled as beams, was able to capture both the nonlinear IOP-induced mean

364   displacement responses of the ONH and the intricate 3D strain patterns in the sclera. In contrast,

365   although the CM employed six constitutive parameters and could replicate the nonlinear

366   displacement responses, it failed to capture the 3D strain patterns of the sclera. Previous studies

367   [40, 43] have also reported similar depth-dependent radial strain patterns in the porcine lamina

368   cribrosa and neural tissue, showing significant anterior compression and posterior stretching. This

369   raises the possibility that if the fibrous structures of the lamina cribrosa and neural tissue were also

370   explicitly modeled, similar accurate results could be achieved for these regions. Further, studies
371   have reported that the average meridional strain in the porcine ONH is greater than the
372   circumferential strain [45, 52, 53]. This finding is consistent with the results from the FM, which
373   showed a larger average meridional strain of 0.089 compared to an average circumferential strain
374   of 0.0265. In contrast, the CM indicated more pronounced stretching in the circumferential
375   direction, with average meridional and circumferential strains of 0.017 and 0.042, respectively.
376   This can also be observed in Figure 8. However, we have not highlighted this finding as a main
377   result of our study because it is derived from just one specimen. Nevertheless, it underscores the
378   potential of the FM. These findings highlight that while the CM is effective for modeling large-
379   scale tissue displacements, it is limited in its ability to represent complex 3D deformation patterns.
380   Conversely, the FM shows considerable promise in capturing these detailed strain patterns,
381   emphasizing its potential to provide a more accurate representation of biomechanical behavior in
382   fibrous tissues.

383   In the second stage of our comparison, we focused on strain transmission along each fiber.
384   The FM allows for direct visualization of fiber kinematics and consistently demonstrated smooth
385   strain distribution along each fiber, as evidenced in Figure 9. In contrast, the CM exhibited
386   substantial variation in fiber strain (Figures 9 and 10) due to its inherent kinematic assumptions.
387   To address concerns that the observed "unsmoothness" or variation in fiber strain within the CM
388   was due to discrepancies in tissue-level strain distributions between the continuum and FMs, we
389   introduced the FM with affine deformation (FMAD). This model recalculated fiber strain using
390   the same affine deformation assumption typically applied in continuum kinematics but based the
391   calculation on the 3D strain tensor derived directly from the FM. This approach ensures that the
392   observed strain "unsmoothness" is not merely a result of differences in the macro-level strain
393   distributions between the models. However, even when FMAD was employed to calculate the fiber
394   strain, the "unsmoothness" remained significant, as illustrated in Figures 9 and 10. This persistence
395   of variation suggests that the issue extends beyond simple alignment of tissue-level strains and
396   points to fundamental limitations of the affine deformation assumptions in continuum kinematics.
397   This finding demonstrates the reliability of the FM and underscores the need for a thorough
398   evaluation of the CM's ability to link macroscopic tissue responses with cellular and sub-cellular
399   level activities.

400   We recognize the substantial expertise within the field dedicated to advancing CMs of

401   fibrous soft tissues. To bridge the gap between macroscopic observations and microscale behavior,

402   multiscale CMs based on representative volume elements (RVEs) have been developed [54]. These

403   models diverge from traditional constitutive material models by accounting for fiber-fiber

404   interactions and non-affine deformations, as detailed in [55-57]. The RVE technique employs a

405   two-scale sequential strategy, homogenizing the microscale behavior of discrete RVEs to derive

406   the macroscale CM response. Each RVE, representing a small patch of networked fibers,

407   influences the behavior at every integration point of the broader CM. Although innovative, the

408   RVE method has limitations, especially due to its reliance on the continuum framework, such as

409   the assumption of fiber independence among elements, which prevents fibers from crossing

410   element boundaries or interacting with fibers within adjacent elements. Additionally, the

411   homogeneous loading of RVE faces with displacements derived directly from the macroscopic

412   solution implies an affine assumption for fiber displacements at the boundary, potentially

413   oversimplifying the complex structures and kinematics of real tissues. Therefore, despite

414   advancements made by the RVE method, its intrinsic limitations associated with the continuum

415   framework persist, and we believe that the FM outperforms it, particularly in accurately capturing

416   detailed fiber kinematics and long-range strain transmission in fibrous tissues.

417   It is important to acknowledge several limitations in this study. Firstly, the two models were

418   constructed based on data from a single porcine eye specimen, while the experimental 3D strain

419   patterns for the sclera were derived from human eyes (see Figures 7 and 8). However, consistent

420   depth-dependent variations in radial strain patterns of the lamina cribrosa (LC) and neural tissue

421   (NT) have been observed in both porcine and human specimens, with porcine specimens showing

422   a much larger magnitude of anterior compression and posterior stretching [40, 43, 45, 46].

423   Additionally, human specimens exhibit similar depth-dependent strain patterns in the LC, NT, and

424   PPS [40, 43]. Therefore, we hypothesize that both human and porcine sclera display similar strain

425   patterns, with individual specimen differences more likely to affect strain magnitudes rather than

426   the patterns themselves. This study focused on comparing the strain patterns rather than absolute

427   values, reinforcing the relevance of the results despite the use of different species.

428   Secondly, as previously mentioned in the manuscript, the modulus of fiber, matrix, and the

429   exponential parameters were assumed to be homogeneous throughout the fibrous region and were

430 inversely identified. Assigning heterogeneous properties might improve the match of local strain
431 patterns; however, the current settings already provide a good approximation of global
432 displacement. If we considered these parameters as heterogeneous, defining a suitable distribution
433 of them across the domain would be challenging. Additionally, the inverse fitting process would
434 become extremely complicated, computationally expensive, and difficult to achieve unique
435 solutions based on the currently used IOP-average displacement response. It remains unknown
436 whether using experimentally measured deformation patterns as objectives for inverse modeling
437 would succeed in accurately determining heterogeneous mechanical properties. However, even if
438 such a match were achieved, it would mean that the CM requires much more complex inverse
439 modeling and more material parameters than the FM to match the 3D strain patterns. Moreover, as
440 discussed previously in the manuscript, matching macroscopic strain patterns does not resolve the
441 'unsmoothness' of fiber strains under the affine deformation assumption.

442 Thirdly, the incompressibility assumption commonly used in modeling ONH [13, 19, 21,
443 22, 58-61], and other soft tissues [62-65] has been widely acknowledged. However, experiments
444 have shown that the ONH and sclera exhibit volumetric compression under inflation [45, 66, 67],
445 suggesting a reconsideration of this assumption. Compressibility of the tissue in the simulations
446 could be achieved through tuning the bulk modulus D. However, this would significantly increase
447 the computational burden. It is still unclear whether assuming compressibility would improve the
448 match of strain patterns.

449 Fourthly, the lamina cribrosa and neural tissue are currently modeled as a homogenized
450 continuum with linear and isotropic material properties in both models. Despite the sclera being
451 modeled as anisotropic and non-homogeneous in the CM, this approach did not successfully match
452 the experimental strain patterns. Given these outcomes, we suspect that modeling the lamina
453 cribrosa and neural tissue as a continuum with anisotropic and heterogeneous properties could
454 potentially improve results. Moreover, as discussed elsewhere in the manuscript, we believe that
455 explicitly modeling the fibrous structures of these tissues, like the sclera fibers in the FM, could
456 lead to better accuracy. This exploration will be a focus of our future work.

457 In conclusion, using the ONH as a test case, the FM demonstrates significant advantages
458 over the CM in modeling fibrous tissues, particularly in its ability to accurately capture intricate
459 3D strain patterns and fiber kinematics, which are essential for understanding tissue biomechanics.

460   While the FM has its limitations—such as the use of representative collagen fiber density,

461   exclusion of the hydrated matrix, and assumptions about frictionless interactions and fiber crimp—

462   it still represents a critical step forward in advancing biomechanical modeling. These limitations,

463   as discussed in detail in the paper [1], provide opportunities for future refinement. Despite these

464   challenges, we believe the insights from our study underscore FM's potential and, more

465   ambitiously, its necessity for further development. This model holds promise for studying the

466   biomechanics and mechanobiology of the ONH and other fibrous soft tissue.

5. REFERENCES

[1] M.R. Islam, F. Ji, M. Bansal, Y. Hua, I.A. Sigal, Fibrous finite element modeling of the optic nerve head region, Acta Biomaterialia 175 (2024) 123-137.

[2] S. Resnikoff, D. Pascolini, D. Etya'ale, I. Kocur, R. Pararajasegaram, G.P. Pokharel, S.P. Mariotti, Global data on visual impairment in the year 2002, Bull World Health Organ 82(11) (2004) 844-51.

[3] Y.-C. Tham, X. Li, T.Y. Wong, H.A. Quigley, T. Aung, C.-Y. Cheng, Global Prevalence of Glaucoma and Projections of Glaucoma Burden through 2040: A Systematic Review and Meta-Analysis, Ophthalmology 121(11) (2014) 2081-2090.

[4] G.R. Howell, I. Soto, R.T. Libby, S.W. John, Intrinsic axonal degeneration pathways are critical for glaucomatous damage, Exp Neurol 246 (2013) 54-61.

[5] R.W. Nickells, G.R. Howell, I. Soto, S.W. John, Under pressure: cellular and molecular responses during glaucoma, a common neurodegeneration with axonopathy, Annu Rev Neurosci 35 (2012) 153-79.

[6] H.A. Quigley, E.M. Addicks, W.R. Green, A.E. Maumenee, Optic nerve damage in human glaucoma. II. The site of injury and susceptibility to damage, Arch Ophthalmol 99(4) (1981) 635-49.

[7] H.A. Quigley, Glaucoma: Macrocosm to Microcosm The Friedenwald Lecture, Investigative Ophthalmology & Visual Science 46(8) (2005) 2663-2670.

[8] I.A. Sigal, R.A. Bilonick, L. Kagemann, G. Wollstein, H. Ishikawa, J.S. Schuman, J.L. Grimm, The Optic Nerve Head as a Robust Biomechanical System, Investigative Ophthalmology & Visual Science 53(6) (2012) 2658-2667.

[9] Z. Zhu, S. Waxman, B. Wang, J. Wallace, S.E. Schmitt, E. Tyler-Kabara, H. Ishikawa, J.S. Schuman, M.A. Smith, G. Wollstein, I.A. Sigal, Interplay between intraocular and intracranial pressure effects on the optic nerve head in vivo, Experimental Eye Research 213 (2021) 108809.

[10] J.C. Downs, M.D. Roberts, I.A. Sigal, Glaucomatous cupping of the lamina cribrosa: a review of the evidence for active progressive remodeling as a mechanism, Experimental eye research 93(2) (2011) 133-140.

[11] I.A. Sigal, J.G. Flanagan, C.R. Ethier, Factors Influencing Optic Nerve Head Biomechanics, Investigative Ophthalmology & Visual Science 46(11) (2005) 4189-4199.

[12] A.J. Bellezza, R.T. Hart, C.F. Burgoyne, The optic nerve head as a biomechanical structure: initial finite element modeling, Invest Ophthalmol Vis Sci 41(10) (2000) 2991-3000.

[13] I.A. Sigal, J.G. Flanagan, I. Tertinegg, C.R. Ethier, Predicted extension, compression and shearing of optic nerve head tissues, Experimental Eye Research 85(3) (2007) 312-322.

[14] I.A. Sigal, J.G. Flanagan, I. Tertinegg, C.R. Ethier, Modeling individual-specific human optic nerve head biomechanics. Part II: influence of material properties, Biomech Model Mechanobiol 8(2) (2009) 99-109.

[15] I.A. Sigal, J.G. Flanagan, I. Tertinegg, C.R. Ethier, Modeling individual-specific human optic nerve head biomechanics. Part I: IOP-induced deformations and influence of geometry, Biomechanics and Modeling in Mechanobiology 8(2) (2009) 85-98.

[16] I.A. Sigal, H. Yang, M.D. Roberts, C.F. Burgoyne, J.C. Downs, IOP-induced lamina cribrosa displacement and scleral canal expansion: an analysis of factor interactions using parameterized eye-specific models, Invest Ophthalmol Vis Sci 52(3) (2011) 1896-907.

[17] I.A. Sigal, H. Yang, M.D. Roberts, J.C. Downs, Morphing methods to parameterize specimen-specific finite element model geometries, Journal of Biomechanics 43(2) (2010) 254-262.

[18] S.L.Y. Woo, A.S. Kobayashi, W.A. Schlegel, C. Lawrence, Nonlinear material properties of intact cornea and sclera, Experimental Eye Research 14(1) (1972) 29-39.

[19] R. Grytz, K. Krishnan, R. Whitley, V. Libertiaux, I.A. Sigal, C.A. Girkin, J.C. Downs, A mesh-free approach to incorporate complex anisotropic and heterogeneous material properties into eye-specific finite element models, Computer Methods in Applied Mechanics and Engineering 358 (2020) 112654.

513 [20] R. Grytz, G. Meschke, J.B. Jonas, The collagen fibril architecture in the lamina cribrosa and
514 peripapillary sclera predicted by a computational remodeling approach, Biomechanics and Modeling in
515 Mechanobiology 10(3) (2011) 371-382.
516 [21] A. Karimi, R. Grytz, S.M. Rahmati, C.A. Girkin, J.C. Downs, Analysis of the effects of finite element type
517 within a 3D biomechanical model of a human optic nerve head and posterior pole, Computer Methods
518 and Programs in Biomedicine 198 (2021) 105794.
519 [22] A. Karimi, S.M. Rahmati, R. Razaghi, C.A. Girkin, J. Crawford Downs, Finite element modeling of the
520 complex anisotropic mechanical behavior of the human sclera and pia mater, Computer Methods and
521 Programs in Biomedicine 215 (2022) 106618.
522 [23] A.P. Voorhees, N.J. Jan, I.A. Sigal, Effects of collagen microstructure and material properties on the
523 deformation of the neural tissues of the lamina cribrosa, Acta Biomaterialia 58 (2017) 278-290.
524 [24] L. Zhang, J. Albon, H. Jones, C.L.M. Gouget, C.R. Ethier, J.C.H. Goh, M.J.A. Girard, Collagen
525 Microstructural Factors Influencing Optic Nerve Head Biomechanics, Investigative Ophthalmology & Visual
526 Science 56(3) (2015) 2031-2042.
527 [25] H.G. Kollech, A. Ayyalasomayajula, R. Behkam, E. Tamimi, K. Furdella, M. Drewry, J.P. Vande Geest, A
528 Subdomain Method for Mapping the Heterogeneous Mechanical Properties of the Human Posterior
529 Sclera, Front Bioeng Biotechnol 7 (2019) 129.
530 [26] A. Gogola, N.J. Jan, B. Brazile, P. Lam, K.L. Lathrop, K.C. Chan, I.A. Sigal, Spatial Patterns and Age-
531 Related Changes of the Collagen Crimp in the Human Cornea and Sclera, Invest Ophthalmol Vis Sci 59(7)
532 (2018) 2987-2998.
533 [27] A. Gogola, N.J. Jan, K.L. Lathrop, I.A. Sigal, Radial and Circumferential Collagen Fibers Are a Feature of
534 the Peripapillary Sclera of Human, Monkey, Pig, Cow, Goat, and Sheep, Invest Ophthalmol Vis Sci 59(12)
535 (2018) 4763-4774.
536 [28] N.J. Jan, K. Lathrop, I.A. Sigal, Collagen Architecture of the Posterior Pole: High-Resolution Wide Field
537 of View Visualization and Analysis Using Polarized Light Microscopy, Invest Ophthalmol Vis Sci 58(2) (2017)
538 735-744.
539 [29] B. Yang, B. Brazile, N.J. Jan, Y. Hua, J. Wei, I.A. Sigal, Structured polarized light microscopy for collagen
540 fiber structure and orientation quantification in thick ocular tissues, J Biomed Opt 23(10) (2018) 1-10.
541 [30] B. Yang, N.J. Jan, B. Brazile, A. Voorhees, K.L. Lathrop, I.A. Sigal, Polarized light microscopy for 3-
542 dimensional mapping of collagen fiber architecture in ocular tissues, J Biophotonics 11(8) (2018)
543 e201700356.
544 [31] P.-Y. Lee, H. Schilpp, N. Naylor, S.C. Watkins, B. Yang, I.A. Sigal, Instant polarized light microscopy pi
545 (IPOLπ) for quantitative imaging of collagen architecture and dynamics in ocular tissues, Optics and Lasers
546 in Engineering 166 (2023) 107594.
547 [32] P.-Y. Lee, B. Yang, Y. Hua, S. Waxman, Z. Zhu, F. Ji, I.A. Sigal, Real-time imaging of optic nerve head
548 collagen microstructure and biomechanics using instant polarized light microscopy, Experimental Eye
549 Research 217 (2022) 108967.
550 [33] F. Ji, M. Quinn, Y. Hua, P.Y. Lee, I.A. Sigal, 2D or not 2D? Mapping the in-depth inclination of the collagen
551 fibers of the corneoscleral shell, Exp Eye Res 237 (2023) 109701.
552 [34] F. Ji, M. Bansal, B. Wang, Y. Hua, M.R. Islam, F. Matuschke, M. Axer, I.A. Sigal, A direct fiber approach
553 to model sclera collagen architecture and biomechanics, Experimental Eye Research 232 (2023) 109510.
554 [35] Y. Lanir, Multi-scale Structural Modeling of Soft Tissues Mechanics and Mechanobiology, Journal of
555 Elasticity 129(1) (2017) 7-48.
556 [36] B. Wang, Y. Hua, B.L. Brazile, B. Yang, I.A. Sigal, Collagen fiber interweaving is central to sclera stiffness,
557 Acta Biomater 113 (2020) 429-437.
558 [37] A.P. Voorhees, N.J. Jan, Y. Hua, B. Yang, I.A. Sigal, Peripapillary sclera architecture revisited: A
559 tangential fiber model and its biomechanical implications, Acta Biomater 79 (2018) 113-122.

560 [38] N.J. Jan, J.L. Grimm, H. Tran, K.L. Lathrop, G. Wollstein, R.A. Bilonick, H. Ishikawa, L. Kagemann, J.S.
561 Schuman, I.A. Sigal, Polarization microscopy for characterizing fiber orientation of ocular tissues, Biomed
562 Opt Express 6(12) (2015) 4705-18.

563 [39] T.C. Gasser, R.W. Ogden, G.A. Holzapfel, Hyperelastic modelling of arterial layers with distributed
564 collagen fibre orientations, J R Soc Interface 3(6) (2006) 15-35.

565 [40] E. Pavlatos, Y. Ma, K. Clayson, X.J. Pan, J. Liu, Regional Deformation of the Optic Nerve Head and
566 Peripapillary Sclera During IOP Elevation, Investigative Ophthalmology & Visual Science 59 (2018) 3779 -
567 3788.

568 [41] K.M. Moerman, The Geometry and Image-Based Bioengineering Add-On, The Journal of Source
569 Software 3 (2018) 506.

570 [42] T.M. Inc., MATLAB version: 9.13.0 (R2022b), Natick, Massachusetts: The MathWorks Inc., The
571 MathWorks Inc., 2022.

572 [43] E. Pavlatos, X. Pan, R.T. Hart, P.A. Weber, J. Liu, ONH Deformation in Porcine Eyes Using Ultrasound
573 Speckle Tracking, Investigative Ophthalmology & Visual Science 57(12) (2016) 3568-3568.

574 [44] B. Coudrillier, C. Boote, H.A. Quigley, T.D. Nguyen, Scleral anisotropy and its effects on the mechanical
575 response of the optic nerve head, Biomech Model Mechanobiol 12(5) (2013) 941-63.

576 [45] S. Kwok, Y. Ma, X. Pan, J. Liu, Three-Dimensional Ultrasound Elastography Detects Age-Related
577 Increase in Anterior Peripapillary Sclera and Optic Nerve Head Compression During IOP Elevation, Invest
578 Ophthalmol Vis Sci 64(7) (2023) 16.

579 [46] Y. Ma, E. Pavlatos, K. Clayson, X. Pan, S. Kwok, T. Sandwisch, J. Liu, Mechanical Deformation of Human
580 Optic Nerve Head and Peripapillary Tissue in Response to Acute IOP Elevation, Invest Ophthalmol Vis Sci
581 60(4) (2019) 913-920.

582 [47] F. Kallel, J. Ophir, A Least-Squares Strain Estimator for Elastography, Ultrasonic Imaging 19(3) (1997)
583 195-208.

584 [48] Y. Ma, E. Pavlatos, K. Clayson, S. Kwok, X. Pan, J. Liu, Three-Dimensional Inflation Response of Porcine
585 Optic Nerve Head Using High-Frequency Ultrasound Elastography, J Biomech Eng 142(5) (2020) 0510131-
586 7.

587 [49] L. Anand, S. Govindjee, Continuum Mechanics of Solids, Oxford University Press2020.

588 [50] S.A. Schwaner, B.G. Hannon, A.J. Feola, C.R. Ethier, Biomechanical properties of the rat sclera obtained
589 with inverse finite element modeling, Biomech Model Mechanobiol 19(6) (2020) 2195-2212.

590 [51] J.D. Humphrey, E.R. Dufresne, M.A. Schwartz, Mechanotransduction and extracellular matrix
591 homeostasis, Nat Rev Mol Cell Biol 15(12) (2014) 802-12.

592 [52] B. Coudrillier, J. Tian, S. Alexander, K.M. Myers, H.A. Quigley, T.D. Nguyen, Biomechanics of the Human
593 Posterior Sclera: Age- and Glaucoma-Related Changes Measured Using Inflation Testing, Investigative
594 Opthalmology & Visual Science 53(4) (2012).

595 [53] K.M. Myers, B. Coudrillier, B.L. Boyce, T.D. Nguyen, The inflation response of the posterior bovine
596 sclera, Acta Biomaterialia 6(11) (2010) 4327-4335.

597 [54] M. Dalbosco, T.A. Carniel, E.A. Fancello, G.A. Holzapfel, Multiscale numerical analyses of arterial tissue
598 with embedded elements in the finite strain regime, Computer Methods in Applied Mechanics and
599 Engineering 381 (2021) 113844.

600 [55] B. Agoram, V.H. Barocas, Coupled macroscopic and microscopic scale modeling of fibrillar tissues and
601 tissue equivalents, J Biomech Eng 123(4) (2001) 362-9.

602 [56] P.L. Chandran, V.H. Barocas, Deterministic material-based averaging theory model of collagen gel
603 micromechanics, J Biomech Eng 129(2) (2007) 137-47.

604 [57] T. Stylianopoulos, V.H. Barocas, Volume-averaging theory for the study of the mechanics of collagen
605 networks, Computer Methods in Applied Mechanics and Engineering 196(31) (2007) 2981-2990.

606 [58] C. Boote, I.A. Sigal, R. Grytz, Y. Hua, T.D. Nguyen, M.J.A. Girard, Scleral structure and biomechanics,
607 Progress in Retinal and Eye Research 74 (2020) 100773.

608 [59] I.C. Campbell, S. Lovald, M. Garcia, B. Coudrillier, Biomechanical Properties of the Sclera, in: I.
609 Pallikaris, M.K. Tsilimbaris, A.I. Dastiridou (Eds.), Ocular Rigidity, Biomechanics and Hydrodynamics of the
610 Eye, Springer International Publishing, Cham, 2021, pp. 77-105.
611 [60] B. Coudrillier, C. Boote, H.A. Quigley, T.D. Nguyen, Scleral anisotropy and its effects on the mechanical
612 response of the optic nerve head, Biomechanics and Modeling in Mechanobiology 12(5) (2013) 941-963.
613 [61] R.E. Norman, J.G. Flanagan, I.A. Sigal, S.M.K. Rausch, I. Tertinegg, C.R. Ethier, Finite element modeling
614 of the human sclera: Influence on optic nerve head biomechanics and connections with glaucoma,
615 Experimental Eye Research 93(1) (2011) 4-12.
616 [62] J.M. Guccione, A.D. McCulloch, L.K. Waldman, Passive material properties of intact ventricular
617 myocardium determined from a cylindrical model, J Biomech Eng 113(1) (1991) 42-55.
618 [63] X. He, J. Lu, Explicit consideration of fiber recruitment in vascular constitutive formulation using beta
619 functions, Journal of the Mechanics and Physics of Solids 163 (2022) 104837.
620 [64] X. He, J. Lu, Modeling planar response of vascular tissues using quadratic functions of effective strain,
621 Int J Numer Method Biomed Eng 39(4) (2023) e3653.
622 [65] G.A. Holzapfel, T.C. Gasser, R.W. Ogden, A New Constitutive Framework for Arterial Wall Mechanics
623 and a Comparative Study of Material Models, Journal of elasticity and the physical science of solids 61(1)
624 (2000) 1-48.
625 [66] B. Coudrillier, D.M. Geraldes, N.T. Vo, R. Atwood, C. Reinhard, I.C. Campbell, Y. Raji, J. Albon, R.L. Abel,
626 C.R. Ethier, Phase-Contrast Micro-Computed Tomography Measurements of the Intraocular Pressure-
627 Induced Deformation of the Porcine Lamina Cribrosa, IEEE Trans Med Imaging 35(4) (2016) 988-99.
628 [67] X. Jia, F. Zhang, M. Cao, Z. Pan, K. Liu, D. Zhou, X. Duan, Elevated IOP Alters the Material Properties of
629 Sclera and Lamina Cribrosa in Monkeys, Dis Markers 2022 (2022) 5038847.

630